ADVANCED OPTICAL MATERIALS
www.advopticalmat.de

Unprecedented Thermal Stability of Plasmonic Titanium Nitride Films up to 1400 °C

*Tobias Krekeler, Surya S. Rout, Gnanavel V. Krishnamurthy, Michael Störmer, Mahima Arya, Ankita Ganguly, Duncan S. Sutherland, Sergey I. Bozhevolnyi, Martin Ritter, Kjeld Pedersen, Alexander Yu Petrov, Manfred Eich, and Manohar Chirumamilla**

Titanium nitride (TiN) has emerged as one of the most promising refractory materials for plasmonic and photonic applications at high temperatures due to its prominent optical properties along with mechanical and thermal stability. From a high temperature standpoint, TiN is a substitution for Au and Ag in the visible to near-infrared wavelength range, with potential applications including thermophotovoltaics, thermoplasmonics, hot-electron and high temperature reflective coatings. However, the optical properties and thermal stability of TiN films strongly depend on the growth conditions, such as temperature, partial pressure of the reactive ion gas, ion energy, and substrate orientation. In this work, epitaxial TiN films are grown at 835 °C on an Al_2O_3 substrate using a radio frequency sputtering method. The oxidization behavior of TiN is investigated at 1000 °C under a medium vacuum condition of 2×10^{-3} mbar, which is relevant for practical technical applications, and the thermal stability at 1400 °C under a high vacuum condition of 2×10^{-6} mbar. The TiN film structure shows an unprecedented structural stability at 1000 °C for a minimum duration of 2 h under a medium vacuum condition, and an exceptional thermal stability at 1400 °C, for 8 h under a high vacuum condition, without any protective coating layer. The work reveals, for the first time to the authors' knowledge, that the TiN film structure with columnar grains exhibits remarkable thermal stability at 1400 °C due to low-index interfaces and twin boundaries. These findings unlock the fundamental understanding of the TiN material at extreme temperatures and demonstrate a key step towards fabricating thermally stable photonic/plasmonic devices for harsh environments.

1. Introduction

Refractory metal-based nanostructures that exhibit structural stability at high temperatures have attracted enormous interest in emerging applications such as thermoplasmonics, thermophotovoltaics (TPV), solar-thermal, hot-electron, solar-steam generation applications.[1–19] However, despite the outstandingly high melting point of bulk refractory metals, nanostructures made of these metals are more susceptible to morphological changes at high temperatures than their bulk counterparts. This is mainly due to large surface-to-volume ratios resulting in increased surface energy in nanostructures[20] that drives redox reactions with ambient gases as well as mass diffusion, leading to structural decay. The inherent thermal instability of these nanostructures hinders their targeted applications at temperatures higher than 1200 °C.[21–25] Further, the materials required for high temperature plasmonic/photonic applications are highly challenging. The combination of spectral selectivity and structural stability at high temperatures leaves only in a tiny subset of available choices of materials.

Dr. T. Krekeler, Dr. S. S. Rout, Dr. M. Ritter
Electron Microscopy Unit
Hamburg University of Technology
Eissendorfer Strasse 42, 21073 Hamburg, Germany

G. V. Krishnamurthy, Dr. M. Störmer, Dr. A. Y. Petrov, Prof. M. Eich
Institute of Materials Research
Helmholtz-Zentrum Geesthacht Centre for Materials and Coastal Research
Max-Planck-Strasse 1, 21502 Geesthacht, Germany

The ORCID identification number(s) for the author(s) of this article can be found under https://doi.org/10.1002/adom.202100323.

DOI: 10.1002/adom.202100323

Dr. M. Arya, A. Ganguly, Dr. A. Y. Petrov, Prof. M. Eich, Dr. M. Chirumamilla
Institute of Optical and Electronic Materials
Hamburg University of Technology
Eissendorfer Strasse 38, 21073 Hamburg, Germany
E-mail: manohar.chirumamilla@tuhh.de

Prof. D. S. Sutherland
Interdisciplinary Nanoscience Center (iNANO) and iMAT
Aarhus University
Gustav Wieds Vej 14, Aarhus 8000, Denmark

Prof. S. I. Bozhevolnyi
Centre for Nano Optics
University of Southern Denmark
Campusvej 55, Odense 5230, Denmark

Prof. K. Pedersen
Department of Physics and Nanotechnology
Aalborg University
Skjernvej 4A, Aalborg 9220, Denmark

Dr. A. Y. Petrov
ITMO University
49 Kronverskii Avenue, Saint Petersburg 197101, Russia

Among the alternative refractory metals, titanium nitride (TiN) attracts increasing attention due to its chemical and thermal stability.[26–29] It is a transition-metal nitride with refractory ceramic properties and a high melting point of 2930 °C, and is compatible with complementary metal-oxide-semiconductor (CMOS) technology.[30] The high hardness and wear/corrosion resistance[31,32] of TiN are effectively utilized to coat cutting tools, thereby increasing their performance and machining durability. TiN, however, also possesses unique optical properties, similar to those of Au in the visible-near infrared regions.[33,34] In fact, TiN is the only material that can provide structural stability and Au-like optical response at high temperatures.

TiN can grow epitaxially on single crystalline Al_2O_3 and MgO substrates with uniformly textured surfaces and a low roughness.[35,36] TiN usually contains crystalline grains elongated in the growth direction, i.e., exhibits a columnar grain structure. TiN has potentials in high temperature applications, such as catalysis,[2] non-contact based high temperature measurement,[27] transducers in heat-assisted magnetic recording (HAMR) data storage,[37–39] thermoplasmonic applications,[40] and TPV.[41] Particularly, in TPV applications, nanostructures should provide spectrally selective optical functionality at temperatures above 1400 °C in order to use high bandgap PV cells, e.g., GaSb. However, it is quite challenging to stabilize the nanostructures at these conditions when the materials are in their pure form, i.e., without doping or alloying the materials.[42] But, alloyed/doped materials suffer from a significant trade-off between optical losses and thermal stability. For instance, TiAlN exhibits excellent oxidization stability at high temperatures compared to TiN, however, it is a highly lossy metal in the visible-near infrared regions.[5,43] Thus, stabilizing the nanostructures without altering their optical/thermal functionality is in high demand. Although there have been detailed studies on the growth of epitaxial TiN,[33,44,45] information on structural properties and thermal stability at extreme temperatures (>1200 °C) is not readily available.

Improving the thermal stability of nanostructures is a long-lasting quest in terms of fundamental research and practical applications. In recent years,[46–50] a grain-boundary engineering concept has been developed to improve the thermal/mechanical/electrical properties of the materials via kinetic and thermodynamic stabilizations. Kinetic and thermodynamic stabilizations can be accomplished by minimizing the grain boundary mobility and reducing the excess grain boundary energy, respectively. Importantly, introducing coherent twin boundaries can improve the structural stability at high temperatures.[51–53] The interfacial energies of twin boundaries are remarkably lower than incoherent grain boundaries, i.e., ≈10× less,[54,55] because of less distorted coordination spheres and fewer crystal lattice defects at twin boundaries. Grain boundaries without a defined common lattice plane show a less ordered arrangement of atoms resulting in a much higher concentration of line defects, which are known as pathways for fast atom diffusion in metals.[56] This diffusion along the disordered grain boundaries may result in rapid grain growth until the formation of stable facets with low interfacial energies, like twin boundaries, slowing the migration of atoms across the boundary and movement of lattice dislocations.[51,57,58] Materials such as borides, carbides, and nitrides become stronger by introducing the twin boundaries.[59–61] Especially in face-centered-cubic (fcc) metals, such as Cu, Ni, TiN, etc., stacking faults or coherent twin boundaries can be easily formed[62–65] under thermal annealing. However, the role of twin boundaries in the thermal stability of TiN structures remained so far unclear.

Herein, we show the effect of columnar grains together with twin boundaries and low-index interfaces on the thermal stability of epitaxially grown TiN film structures at temperatures up to 1400 °C. Low-index interfaces provide low energy surfaces, which are crucial for minimizing the grain growth at high temperatures.[66,67] Epitaxial growth of TiN on Al_2O_3 {0001} and Si {100} substrates along {111} and {100} planes, respectively, has been observed before despite the significant mismatch in lattice parameters.[5,35,68,69] The surface energies of TiN increase in the order S(100) < S(110) < S(111) as expected from ionic compounds.[70] In situ optical properties of the TiN films up to 1000 °C under medium vacuum conditions (3×10^{-3} mbar), and ex situ optical properties after annealing up to 1400 °C under high vacuum conditions (2×10^{-6} mbar) are investigated. Most of the refractory metals are prone to oxidization when they are heat treated under O_2 environments. The plasmonic/photonic nanostructures made up of refractory metals will be usually operated under an inert gas atmosphere or medium/high vacuum conditions at high temperatures. Thus, the thermal stability of the TiN structures was evaluated at high temperatures under medium/high vacuum conditions.

TiN films show the remarkable structural stability, when there is no protective coating layer, under medium and high vacuum conditions, respectively. Unprecedented thermal stability of the plasmonic TiN film structure is demonstrated for the duration of 120 h at 1000 °C and 8 h at 1400 °C. Annealing the TiN film structure at a high temperature of 1400 °C contributes to the formation of low-index interfaces and twin boundaries. To the best of our knowledge, our work provides for the first time comprehensive and unambiguous observation of the thermal stability of thin TiN film structures at 1400 °C due to the formation of low-index interfaces and twin boundaries. The results obtained open new perspectives for significantly improving the structural/thermal stability of the refractory metals at extreme temperatures by tailoring the grain boundary interfaces.

2. Results and Discussion

The cross-sectional high-resolution transmission electron microscopy (HRTEM) image of **Figure 1**A shows an 80 nm TiN film structure grown on single crystalline Al_2O_3 substrate. The inset shows the schematic of the structure. A magnified view around the interface of TiN and Al_2O_3 substrate is shown in HRTEM, Figure 1B. A smooth interface is observed between TiN film and Al_2O_3 substrate, and no pinholes, voids, or pores are observed in TiN. The as-fabricated TiN film shows domains (Figure S1, Supporting Information, and Figure 3D), which indicates that TiN is in the nanocrystalline state. Figure 1C shows the selected area electron diffraction (SAED) pattern of the as-fabricated structure taken at the interface (marked on Figure 1B). The SAED pattern clearly establishes

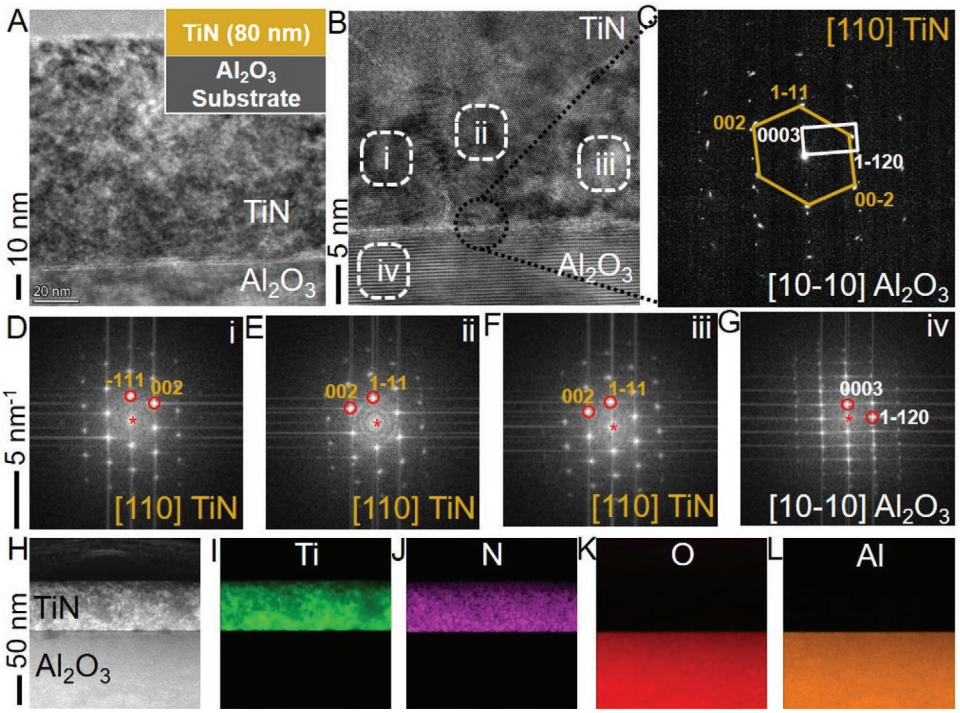

Figure 1. Morphology and epitaxial growth of TiN. A) HRTEM image of an 80 nm TiN film grown on single crystalline Al_2O_3 (0001) substrate. Note that a protective carbon layer is deposited before FIB milling to protect the TiN film during specimen preparation. Inset shows the schematic of the structure. B) Magnified view of (A) at the interface. C) Selected area diffraction (SAED) obtained at the interface between TiN and Al_2O_3 showing the epitaxial relationship. D–G) FFTs of the selected areas in (B). STEM HAADF image H) of as-fabricated TiN film structure, and element maps I–L) of Ti, N, O, and Al.

cube-on-hexagonal alignment between TiN and Al_2O_3 substrate, which confirms the epitaxial growth of TiN on crystalline Al_2O_3. The hetero-epitaxial relationship is (111) TiN ‖ (0001) Al_2O_3 and [110] TiN ‖ [10-10] Al_2O_3 due to the compatibility between the cubic lattice of TiN and hexagonal lattice of Al_2O_3. Fast Fourier transforms (FFTs) of the selected areas marked on Figure 1B, at different grains of the TiN structure, are shown in Figure 1D–F. Figure 1G shows the FFT of the Al_2O_3 substrate. The FFT patterns show the growth of cubic-TiN film along [111] direction with the (111) planes of the TiN film parallel to the (0001) oriented Al_2O_3 substrate. Further, the FFTs (Figure S2, Supporting Information) taken at a different location of the film shows epitaxial growth of TiN on Al_2O_3 substrate, confirming the homogeneity of the epitaxial film growth.

The X-ray diffraction (XRD) pattern (Figure S3, Supporting Information, and Figure 5) of the as-deposited TiN film, shows two reflexes at 36.5° and 41.6°, corresponding to (111) and (0006) planes of cubic-TiN and the Al_2O_3 single crystalline substrate, respectively. The total integrated X-ray intensity over a large area, which covers a vast number of grains, shows that TiN is grown in [111] direction on the Al_2O_3 substrate, which is consistent with the relationship ((111) TiN ‖ (0001) Al_2O_3) observed in HRTEM investigations. An asymmetric-φ scan of the as-fabricated structure is shown in Figure 5B and the inset of Figure S3. The φ-scans were performed to investigate the in-plane epitaxial relationship between TiN and Al_2O_3. The 2θ was aligned to (200) reflection of TiN, and with respect to the interplanar angle between (111) and (200) planes of TiN, and the off-plane tilt angle (χ) was fixed to 54.7°. A sixfold symmetry with a 60° separation is observed in the in-plane φ-scan, corresponding to the (200) reflexes and revealing the presence of epitaxially grown TiN on hexagonal Al_2O_3 substrate. Figure 1H–L shows the high-angle annular dark-field scanning transmission electron microscopy (HAADF-STEM) image and element maps created by energy-dispersive X-ray spectroscopy (EDS) analyses of the as-fabricated TiN structure. The spectrum images clearly show the elements, Ti, N, O, and Al, in their respective layers, and the as-fabricated TiN is free from any O_2 contamination during the growth process (Figure 1K).

Figure 2A,B shows the measured temperature-dependent complex dielectric permittivities, real (ε_1) and imaginary (ε_2) parts, respectively, of the TiN film at room temperature (RT) and high temperatures up to 1000 °C, under a medium vacuum condition of 3×10^{-3} mbar pressure.[71] The complex dielectric permittivities are evaluated by fitting a Drude-Lorentz oscillator model (Equation 1), where conduction electron contribution and interband transitions are expressed by Drude and Lorentz terms, respectively.[72]

$$\varepsilon(\omega) = \varepsilon_1 + i\,\varepsilon_2 = \varepsilon_\infty - \frac{\omega_p^2}{\omega^2 + i_{\Gamma D}\omega} + \sum_{j=1}^{2} \frac{\omega_{L,j}^2}{\omega_{0,j}^2 - \omega^2 - i\gamma_j\omega} \quad (1)$$

where, ε_∞, ω_p, Γ_D, γ_j, are the background dielectric constant accounting for higher energy interband transitions outside the probed energy spectrum, plasma frequency, collision frequency, and Lorentz oscillator damping factor, respectively. At RT, TiN shows a highly metallic nature (large negative ε_1) and low losses (low ε_2), consistent with the results published elsewhere,[73]

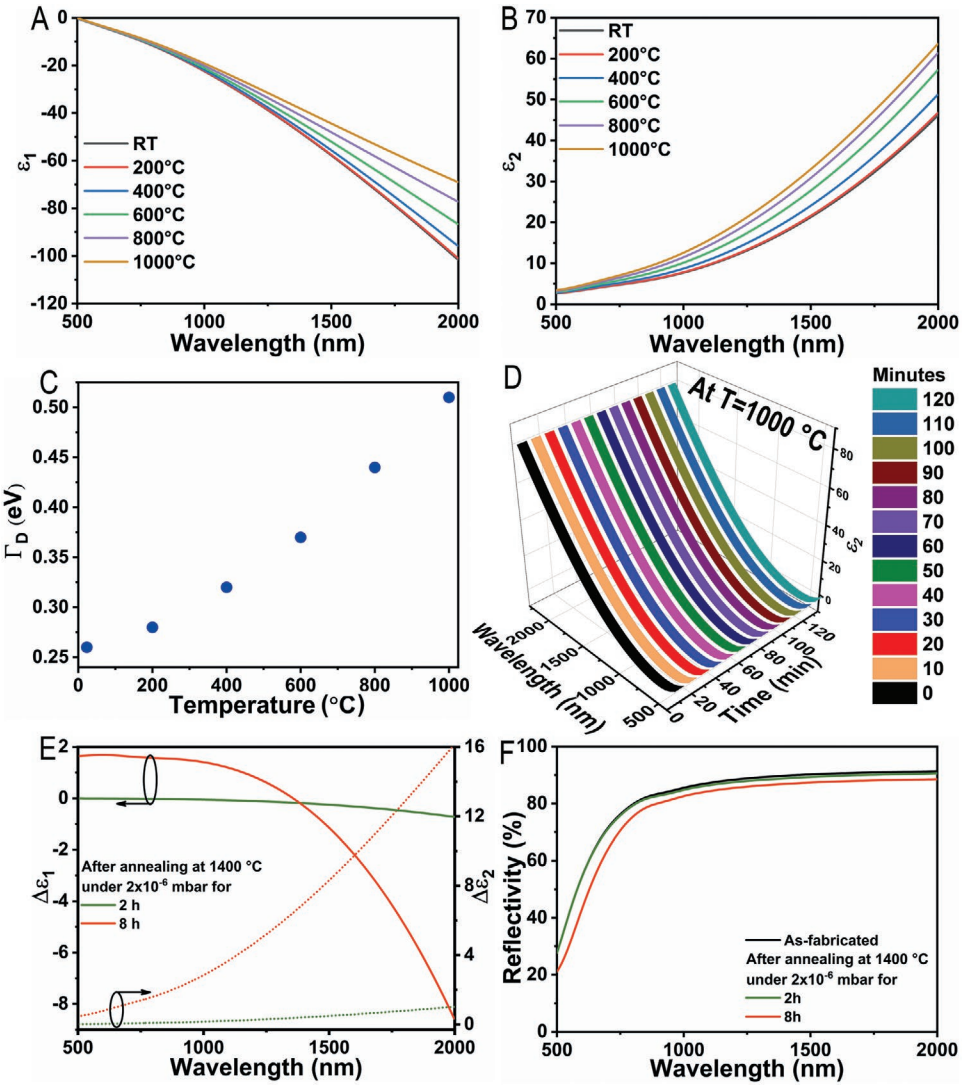

Figure 2. In situ and ex situ optical properties of TiN films at temperatures, up to 1400 °C. A,B) In situ real and complex part of the dielectric permittivities ε_1 and ε_2, respectively, of an 80 nm TiN film at room temperature, and increasing temperatures, up to 1000 °C under 2×10^{-3} mbar vacuum pressure. C) Collision frequency of TiN as a function of temperature (conditions as in (A,B)). D) In situ complex dielectric permittivity ε_2 of the TiN film at 1000 °C, under 2×10^{-3} mbar vacuum pressure, during 2 h annealing procedure. E) Ex situ relative complex dielectric permittivities ε_1 and ε_2 of the TiN film after annealing at 1400 °C for 2 and 8 h, under 2×10^{-6} mbar vacuum pressure, with respect to the as-fabricated structure; and F) the corresponding specular reflectivity of the TiN film.

where ε_1 and ε_2 represent metallicity and optical losses in the material, respectively. When the temperature is raised from RT to 1000 °C, ε_1 shows a decrement in magnitude whereas ε_2 shows an increment. As the temperature rises, the electron–phonon collision frequency monotonically increases via increased population density of phonons (Figure 2C). The collision frequency has an influence on both the real and imaginary part of permittivity. For the case when the excitation frequency is larger than collision frequency, ε_2 and ε_1 are increasing with temperature. The temperature-dependent parameters of the Drude-Lorentz model are listed in Table S1 (Supporting Information), and real and complex dielectric permittivities (ε_1 and ε_2, respectively) at RT and high temperatures, up to 1000 °C, are listed in Table S2 (Supporting Information).

In order to investigate the oxidization resistance, the TiN thin film structure is heated at 1000 °C, under a medium vacuum condition of 3×10^{-3} mbar pressure, for 2 h inside the Linkam heating chamber, and the complex dielectric permittivities of TiN were measured at 10 min intervals. In oxidizing environments, TiN can react with O_2 and form nonstoichiometric phases of TiON or TiO_2, such as TiO_xN_y or TiO_{2-x}, respectively.[74–76] Figure 2D shows the ε_2 versus annealing duration of the TiN structure at 1000 °C. Although the partial O_2 pressure in the vacuum chamber is 4.2×10^{-4} mbar (assumed to be 21% of vacuum pressure),[77] no change in ε_2 is observed throughout the 2 h annealing at 1000 °C, which highlights the spectral/thermal stability of the TiN under medium vacuum conditions. Also, note that no change in the visual appearance of the substrate is observed (Figure S4B, Supporting Information). The XRD spectra (Figure S4C, Supporting Information) taken after annealing at 1000 °C for 2 h shows no sign of nonstoichiometric phases of TiON or TiO_2 formation, except a change

in TiN grain size. It is changed from 18 nm to 23 nm, for as-fabricated to the structure annealed at 1000 °C for 2 h, respectively. In order to compare the oxidization stability of TiN with the highest melting point refractory metal W, an 80 nm thick W structure was annealed at 1000 °C for 2 h under 3×10^{-3} mbar pressure. After cooling to RT, the color of the W structure surface is transformed to blue (Figure S4E, Supporting Information), and the XRD pattern reveals the formation of tungsten oxide $WO_{2.9}$. In order to test the long-term stability of the TiN structure at 1000 °C, a TiN structure is annealed for 120 h under a high vacuum condition of 2×10^{-6} mbar pressure (Figure S5, Supporting Information). The reflectivity spectrum clearly shows an improvement in reflectivity throughout the spectral range in accordance with the XRD spectrum showing a rise in grain size, and no other residues such as non-stoichiometric phases of TiON or TiO_2 are observed.

To validate the thermal stability of the TiN at even higher temperatures, TiN structures were annealed at 1400 °C for up to 8 h under a high vacuum condition of 2×10^{-6} mbar pressure. Figure 2E shows the ex situ relative complex dielectric permittivities ε_1 and ε_2 of the TiN structure after annealing at 1400 °C for 2 h and 8 h, under 2×10^{-6} mbar vacuum pressure, with respect to the as-fabricated structure. After annealing the TiN structure at 1400 °C for 2 h, no change in the relative magnitude of ε_1 and ε_2 was noticed. The corresponding ex-situ reflectivity spectra of the TiN structures are shown in Figure 2F, where the structure annealed for 2 h shows no variation in reflectivity compared to the as-fabricated structure. However, after annealing for 8 h at 1400 °C, a substantial change in ε_1 and ε_2 is observed. The ex situ reflectivity (Figure 2F) of the TiN structure annealed at 1400 °C for 8 h shows a slightly reduced reflectivity compared to the as-fabricated structure, which is the result of the increased ε_2 (Figure 2E). This increase can be due to many factors, such as the formation of TiON or TiO_2 on the top surface of the structure due to the partial O_2 pressure in the vacuum chamber, and/or changes in the microstructure of the TiN film, and it will be discussed in the next section. Further, the thermal stability of TiN at 1400 °C is compared with W. The W structure with an 80 nm thickness is annealed at 1400 °C for 2 h under 2×10^{-6} mbar vacuum pressure. After cooling to RT, the W structure is completely transformed into translucent material (Figure S6, Supporting Information) even though the partial O_2 pressure in the chamber is in the order of $\times 10^{-7}$ mbar. W tends to form W-oxides and sublimates at temperatures above 1000 °C.[4,78,79]

To investigate the underlying physical reasons behind the increment of ε_2 due to heat treatment at 1400 °C (Figure 2E), structural characterizations such as SEM, XRD, and STEM analyses are performed. **Figure 3** shows the normal-incidence SEM images of the TiN structure for as-fabricated and annealed (at 1400 °C for 2 h and 8 h) structures. The as-fabricated TiN structure shows multiple nanocrystalline domains (Figure 3D, Figure S1, Supporting Information) with an average grain size of 18 nm as defined from XRD analyses (**Table 1**). However, all these nanocrystalline grains are grown epitaxially on Al_2O_3 with the hetero-epitaxial relationship as (111) TiN ‖ (0001) Al_2O_3 and [110] TiN ‖ [10-10] Al_2O_3 (Figures 1 and 5, Figures S2 and S3, Supporting Information). The TiN grain size was calculated using the Scherrer formula,[80,81] taking into account the (111) reflex of TiN. Upon annealing of the structure at 1400 °C for 2 h, grain growth occurred, and large crystalline grains with an average size of 73 nm were formed.

Figure 4A shows the HRTEM image of the TiN structure, and a low magnification TEM image is shown in Figure S7

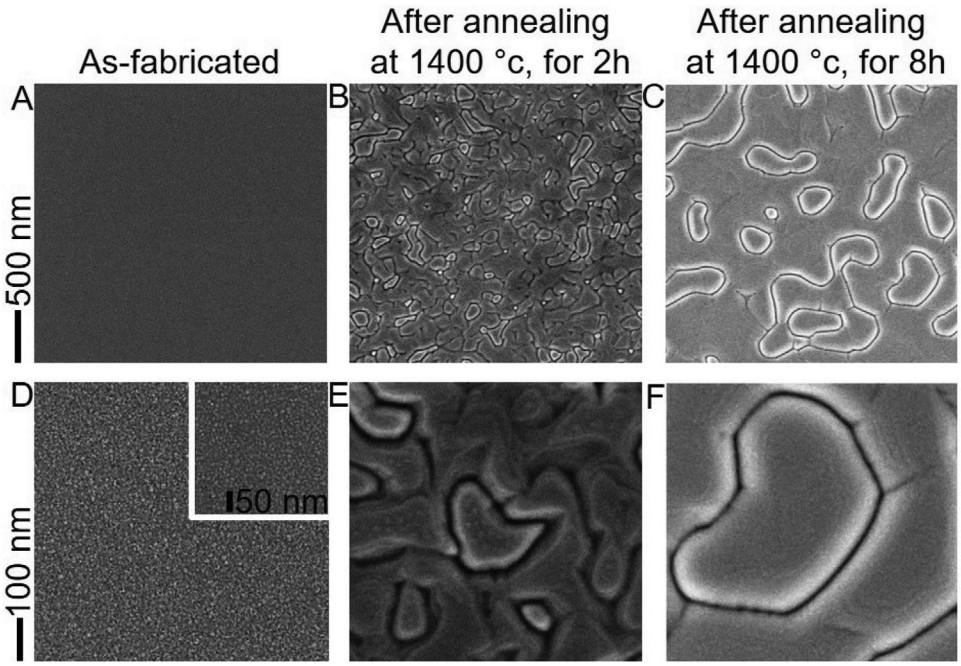

Figure 3. Structural changes in TiN film after heat treating at 1400 °C, under a high vacuum condition of 2×10^{-6} mbar. A–C) Normal-incidence SEM images of the 80 nm TiN films,A) as-fabricated and B,C) annealed at 1400 °C for 2 and 8 h, respectively, under 2×10^{-6} mbar vacuum pressure; D–F) the corresponding magnified views.

Table 1. Grain size, 2θ, lattice parameter d, and unit cell parameter a of as-fabricated and the structure annealed at 1400 °C for 2 h and 8 h under 2×10^{-6} mbar vacuum pressure.

TiN	Grain size [nm]	2θ [°]	d [Å]	a [Å]
As-fabricated	18	36.51	2.459	4.259
After annealing at 1400 °C for 2 h	76	36.65	2.45	4.243
After annealing at 1400 °C for 8 h	111	36.65	2.453	4.249

(Supporting Information). A smooth interface between TiN and Al_2O_3 is observed, and no defects, such as voids or pores, are observed in TiN after annealing at 1400 °C for 2 h. Figure 4B shows the interface of the selected area on Figure 4A, where no interdiffusion is perceived. The TiN lattice spacing in [111] direction is 2.4 Å (inset of Figure 4B), which is also confirmed by XRD analysis (Table 1). The XRD pattern of the TiN structure after annealing at 1400 °C for 2 h, **Figure 5**A-red trace, clearly shows a highly intense and narrow peak at 36.6°, which can be attributed to the increased grain size and improved quality of the TiN epilayer. An asymmetric in-plane φ-scan in Figure 5B-red trace with narrow reflections of (200) also confirms the enhanced quality of the TiN epilayer. The FFT patterns in Figure 4C,D were taken on either side of the grain boundary, from regions marked in Figure 4A. The FFT pattern, Figure 4C, shows the epilayer of cubic TiN grown in [111] direction on the hexagonal crystalline structure of the Al_2O_3 substrate (Figure 4E). In Figure 4D, the FFT pattern shows that the normal stacking sequence of (111) plane of the cubic TiN crystal is mirrored, indicating the formation of a coherent twin boundary between these grains. A Moiré pattern is observed at the twin boundary (Figure 4A) since the twin boundary is not resolved atomically in the {2-1-1} or (10-1).[9,55,82]

During the 2 h annealing of the TiN structure at 1400 °C, grain growth takes place due to thermal activation, and the formation of twin boundaries is observed as a consequence of the grain boundary relaxation. The as-fabricated nanocrystalline TiN structure exhibits low thermal stability owing to the high volume fraction of the grain boundaries, which raise the interfacial Gibbs excess free energy. At high temperatures, the driving force for the grain growth originates from the reduction of Gibbs excess free energy, allowing diffusion at the grain boundaries and grain coarsening. The driving force for grain growth is proportional to the grain boundary energy and inversely proportional to the grain size.[83] Since, TiN is grown at 835 °C on Al_2O_3 substrate and due to different thermal expansion coefficients of TiN and Al_2O_3, 9.35×10^{-6}/°C and 8.4×10^{-6}/°C, respectively,[84] after cooling down to RT the TiN film will experience a tensile strain. Further, in a large mismatched lattices (8.7%) of TiN and Al_2O_3, dislocations will be nucleated within a few monolayers and epitaxial growth is achieved by the domain

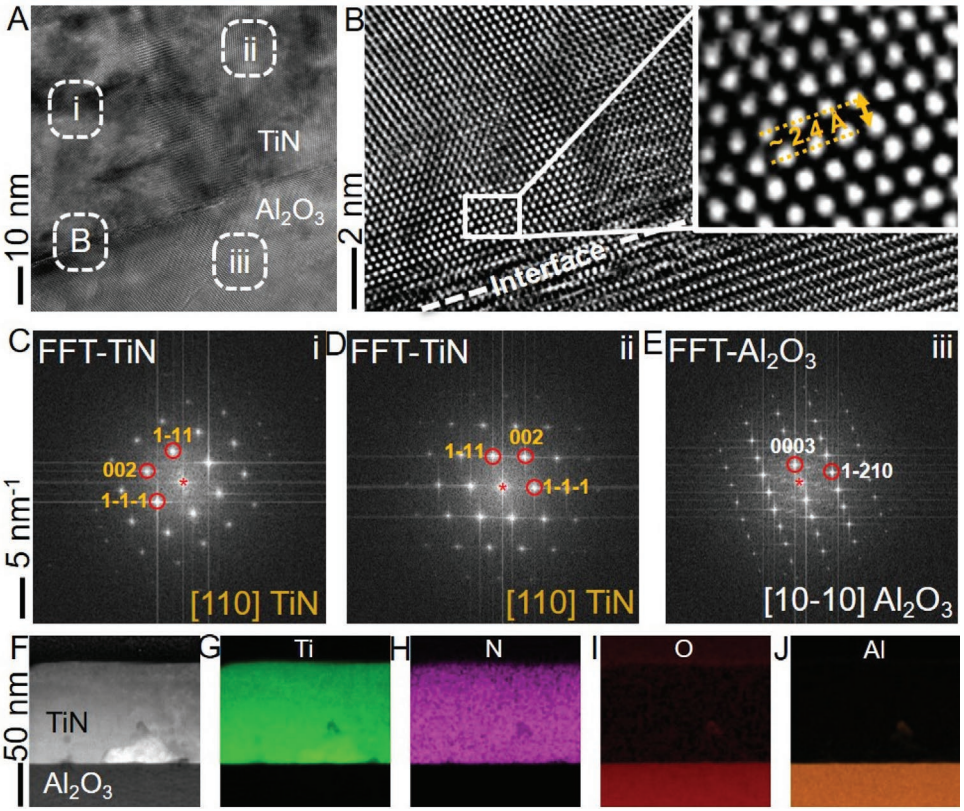

Figure 4. HRTEM, FFTs, and elemental analysis of an 80 nm TiN film annealed at 1400 °C for 2 h. A) HRTEM image epitaxially grown TiN film on Al_2O_3 substrate. B) Magnified view of the (A) at the TiN film on Al_2O_3. Inset shows that the TiN lattice parameter along [111] direction is 2.4 Å. C–E) FFTs of the selected areas in (A). F) STEM-HAADF image of an 80 nm TiN film structure annealed at 1400 °C for 2 h, under 2×10^{-6} mbar vacuum pressure, and G–J) element maps of Ti, N, O, and Al.

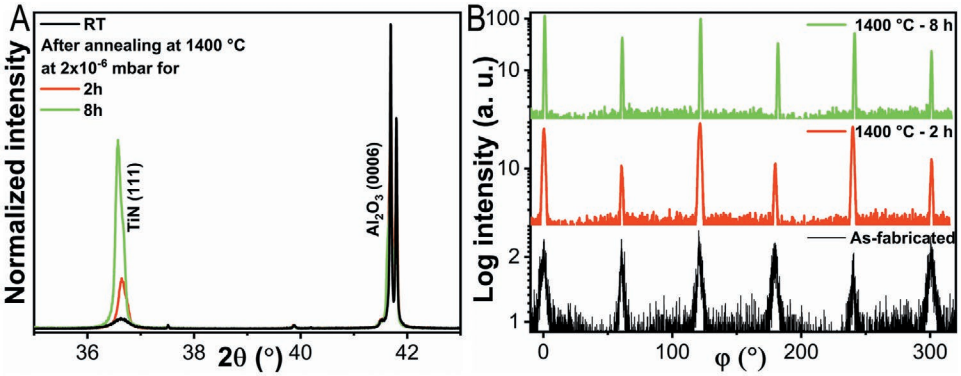

Figure 5. XRD analysis of the TiN film before and after annealing at 1400 °C. A) XRD patterns of the TiN film for as-fabricated and annealed at 1400 °C for 2 h and 8 h under 2×10^{-6} mbar vacuum pressure. B) Asymmetric-φ scan patterns of the structures for as-fabricated and annealed at 1400 °C for 2 and 8 h under 2×10^{-6} mbar vacuum pressure, where 2θ was aligned to (200) reflection of TiN. The off-plane tilt angle (χ) was aligned to 54.7°, with respect to the interplanar angle between (111) and (200) planes of TiN.

matching epitaxy.[85,86] During the annealing process, TiN grains grow until twin boundaries are formed.[87–89] After annealing the TiN structure at 1400 °C for 2 h, the number of grain boundaries decreased, and the formation of dense columnar large crystalline grains spanning vertically the entire film thickness was observed, Figure 4A and Figure S7 (Supporting Information). These columnar grains were elongated along the TiN growth direction [111], i.e., normal to the Al_2O_3 substrate. Although most of these grain boundaries are low-index interfaces, some high angular grain boundaries (Figure S7B, Supporting Information) are also observed at the Al_2O_3 interface. It can be understood that 2 h annealing duration at 1400 °C is not enough to form a complete low-index surface. The EDS spectrum images in Figure 4G–J, show the elements Ti, N, O and Al, for the TiN structure annealed at 1400 °C for 2 h. No O content in TiN (Figure 4I), and no diffusion of Ti or N into Al_2O_3 substrate (Figure 4G,H) is observed. When O_2 is reacted with TiN, it can form TiO_xN_y or $TiO_{2-x,}$ which can be easily detected (even with a few nm layer thickness) using spectroscopic ellipsometer or reflectivity measurements. However, after annealing the TiN structure at 1400 °C for 2 h and cooling down to room temperature, no significant changes in the ε_1 and ε_2, and reflectivity (Figure 2E,F) is observed when compared to the as-fabricated TiN structure. The TiN undergoes with the grain growth induced surface modifications, and no additional changes to the surface such as the formation of pores or voids (Figures 3 and 4) are observed after annealing at high temperatures.

Upon annealing the TiN film for 8 h at 1400 °C (Figure 3C,F), large crystalline columnar grains with an average size of 111 nm (Table 1) are observed. The XRD pattern in Figure 5A-green trace clearly shows the increased intensity of (111) TiN reflection, confirming the grain growth in [111] direction. The in-plane φ-scan measurement (Figure 5B-green trace) shows narrow (200) reflexes with a still intact sixfold symmetry, indicating the epitaxial nature of the film is still preserved after annealing it for 8 h. The XRD patterns are in line with the results observed in SEM and TEM investigations and confirm the increased grain size as well as improved quality of the epilayer of TiN.

Figure 6A shows the TEM image of the TiN structure annealed at 1400 °C for 8 h. A smooth interface between the TiN film and Al_2O_3 substrate is seen, and it is free from any defects or inter-diffusion. A magnified view around the grain boundary (selected area on Figure 6A) is shown in the HRTEM image of Figure 6B. The TiN lattice spacing along [111] growth direction is ≈2.4 Å (Figure S8, Supporting Information), which is affirmed by the XRD measurement (Table 1) and highlights the quality of the epitaxial TiN layer after annealing at 1400 °C for 8 h. Figure 6C,D shows the magnified regions marked on Figure 6B, on two sides of the grain boundary, respectively. The FFT pattern in Figure 6F (selected area on Figure 6C) clearly shows that TiN is growing in [111] direction on the single crystalline Al_2O_3 substrate. Whereas Figure 6G (selected area on Figure 6D) shows the (111) mirror symmetry, the normal stacking sequence of (111) plane is mirrored, confirming the existence of coherent twin boundaries.

Twin boundaries are often formed during the cooling ramp of the high temperature annealing process due to the phase change in the crystal. However, after annealing at 1400 °C, no phase change is observed in TiN. Thus, the formation of twin boundaries is associated with the random orientation of TiN (in the as-fabricated nanocrystalline state) during high temperature annealing at 1400 °C along with the grain growth. Therefore, the cooling ramp process will not affect the already formed low-energy twin boundaries.

An overview of the TEM lamella is shown in Figure S9 (Supporting Information), where the inset shows the observed low-index interfaces between the grains. It is apparent that, after annealing the structure at 1400 °C for 8 h, low-index interfaces are formed throughout the TiN film (marked with black dotted lines). While the TiN structure annealed at 1400 °C for 2 h contains a mixture of low-index boundaries and high angular grain boundaries (Figures S7 and S8, Supporting Information). After annealing at 1400 °C for 8 h, the grain size is increased from 76 to 111 nm (Table 1) at the expense of high angular grain boundaries. Due to the coexistence of columnar grains with twin boundaries and low-index interfaces, the average interfacial grain-boundary energy of the TiN structure will be reduced significantly compared to the as-fabricated, and 2 h annealed structures. The grain growth in lateral directions is constrained by the formation of low-energy twin planes and resulting in elongation of the grains along the [111] direction, perpendicular

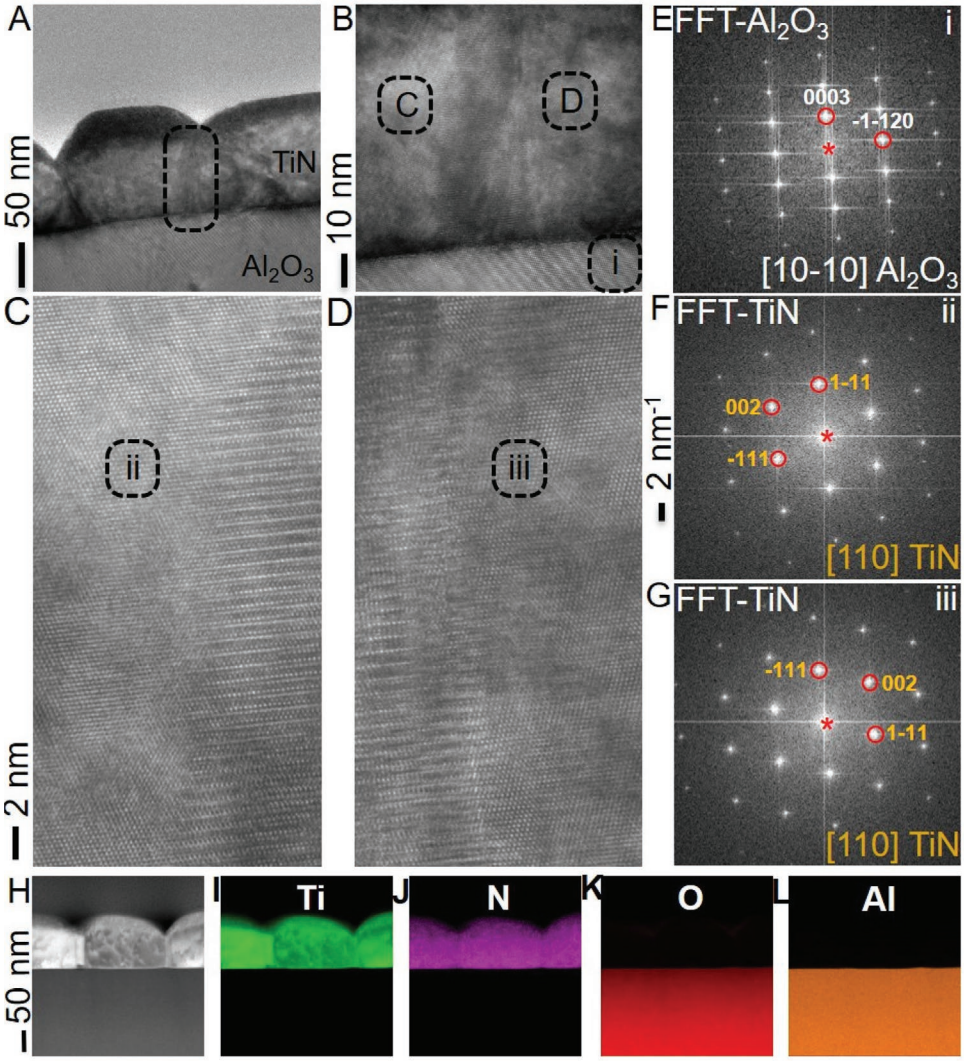

Figure 6. Grain growth and twin boundary formations in TiN film after annealing at 1400 °C for 8 h. A) TEM image of TiN film structure after annealing at 1400 °C for 8 h, under 2×10^{-6} mbar vacuum pressure. B) HRTEM image of (A) around the twin boundary. C,D) Cross-sectional HRTEM images of TiN film before and after the twin boundary, marked in (B). E–G) FFTs of the selected areas on the HRTEM image (B-D). H) STEM HAADF image of an 80 nm TiN film structure annealed at 1400 °C for 8 h, under 2×10^{-6} mbar vacuum pressure, and I–L) element maps of Ti, N, O and Al.

to the substrate. This rises spheroidization of the column tops and contributes to the surface roughness (Figure 6A and Figure S9, Supporting Information). Figure 6I–L shows the EDS spectrum images of the TiN structure after annealing at 1400 °C for 8 h, for the elements Ti, N, O, and Al. Even after 8 h annealing at 1400 °C, O content is not observed in TiN, and Al_2O_3 substrate is free from Ti or N diffusion, or diffusion of Al into TiN. Thus, the change in optical properties of the TiN structure after annealing at 1400 °C for 8 h, i.e., high ε_2 and low reflectivity (Figure 2E,F), is attributed to the surface roughness of the TiN structure due to spheroidization.

3. Conclusion

The thermal stability of plasmonic TiN structures at high temperatures and, under medium and high vacuum conditions is systematically explored. Under a medium vacuum condition of 3×10^{-3} mbar, TiN shows unprecedented structural stability against oxidization when the structure is annealed for a minimum duration of 2 h at 1000 °C. The temperature-dependent optical properties of the TiN structures were evaluated using an in situ ellipsometer. By using the measured optical constants data, the optical response of plasmonic/photonic nanostructures at high temperatures can be easily evaluated.

The TiN structure shows excellent long-term stability for a minimum duration of 120 h at 1000 °C under a high vacuum pressure of 2×10^{-6} mbar. Thermal stability of the TiN structure is evaluated by annealing the structure at 1400 °C under a high vacuum pressure of 2×10^{-6} mbar. After annealing the structure at 1400 °C for 2 h, the nanocrystalline grains in the as-fabricated structure are transformed into textured columnar grains with twin boundaries containing low-index interfaces and high angular grain boundaries, where these grains are highly crystalline and spanned the entire film vertically. A coherent

twin boundary restricts the movement of lattice dislocations, thereby stabilizing the nanostructures at high temperatures.

The TiN structure annealed at 1400 °C for 2 h shows more than 4× increase in grain size, i.e., from 18 nm to 76 nm, due to the existence of a vast number of grain boundaries in the as-fabricated structure. However, further annealing the structure for 6 h (a total of 8 h) at 1400 °C causes a 1.4× further increment in grain size, from 76 to 111 nm, owing to a fewer number of grain boundaries. Since the grain growth primarily depends on the excess interfacial energy, lowering this energy with fewer low-index and twin boundary surfaces minimizes the thermodynamic driving force, thereby reducing the grain growth and stabilizing the nanostructure. Without any protective coating layer, TiN shows unprecedented structural stability under medium and high vacuum conditions, and at elevated temperatures of 1400 °C. The co-existence of columnar grains with low-index interfaces and twin boundaries impedes the grain growth and plays a key role in enhancing the thermal stability of TiN at high temperatures. These findings are expected to lead to new insights, enabling an alternative stabilization strategy for metals without changing the chemistry of the materials, i.e., alloying or doping.

4. Experimental Section

Growth of TiN Film: The TiN film was deposited onto Al_2O_3 (0001) substrate by direct current (DC) magnetron sputter deposition at a base pressure of 3×10^{-7} mbar. The Al_2O_3 substrate was preheated to 835 °C and maintained at this temperature during deposition. A bias power of 390 W was applied for DC sputtering, and Ar and N_2 gases of 20 and 25 SCCM, respectively, were let into the chamber. With a deposition rate of 0.5 nm s^{-1}, an 80 nm TiN film was deposited.

In Situ Ellipsometry: The in-situ temperature-based optical constants of the TiN thin film structures were measured by spectroscopic ellipsometer (Semilab SE-2000), at an incident angle of 70°, in the visible-to-NIR region (500–2100 nm). The spectroscopic ellipsometer was equipped with a CCD spectrograph and InGaAs linear array detector to measure the samples in the wavelength ranges of 198–900 nm and 900–2100 nm, respectively. The TiN sample was mounted onto a heating stage (Linkam Scientific Model TSEL1000V). The heating stage contained a ceramic heating cup, and it was controlled through the Linkam T96-S temperature controller. The heating stage contained two side quartz windows, fixed at an angle of 70°, along the polarizer and analyzer arms of the ellipsometer, and a center quartz window for the sample inspection. The heating stage was connected to a rough vacuum pump, and a medium vacuum pressure of 3×10^{-3} mbar was maintained during high temperature operation. The TiN samples were heated between 20 °C and 1000 °C with a step size of 100 °C and a ramp rate of 40 °C min^{-1}. And at each temperature, the sample was kept for 10 min to achieve thermalization with the heating element, and then measurements were taken. An external water-cooling unit is connected to the heating stage to cool the quartz windows at high operating temperatures.

The optical constants of TiN were fitted using Semilab spectroscopic ellipsometry analyzer (SEA) software using a Drude and two Lorentz oscillators. The thickness of TiN was fixed to 80 nm, and the real and imaginary parts of the complex dielectric functions were extracted.

Reflectivity Measurements: The specular reflectivity spectra of the TiN film structures, for as-fabricated and after annealing at high-temperatures, were measured using a UV–Vis–NIR spectrometer (PerkinElmer Lambda 1050) in the range of 0.5 to 2.0 µm with a wavelength scan step of 5 nm. A labsphere spectralon reflectance standard was used for normalization. The incident light was unpolarized, and the minimum angle of incidence of the system was 8°.

Thermal Stability of TiN Film at 1400 °C: Thermal annealing experiments were performed in a high-temperature vacuum furnace (RD-G WEBB) at 1400 °C and durations up to 8 h under 2×10^{-6} mbar vacuum pressure. The temperature was ramped at a rate of 10 °C min^{-1}.

XRD Measurements: XRD measurements were taken using a Bruker D8 advanced diffractometer equipped with a Lynxeye XE-T, Bruker AXS position sensitive detector, and compact cradle. Cu K_α ($\lambda = 0.15405$ nm) radiation with Bragg Brentano geometry was used to characterize the metamaterial structure. TiN grain size is calculated using Scherrer equation:[80,81]

$$\text{Grain size} = \frac{K\lambda}{\beta \cos\theta} \tag{2}$$

where K, λ, β and θ are corresponding to dimensionless shape factor, X-ray wavelength ($\lambda_{Cu\ K\alpha}$ = 0.154055 Å), FWHM of the fitted peak in radians and Bragg angle in degrees, respectively.

Morphology and Elemental Analysis: Cross-sectional TEM samples were prepared with a focused-ion beam (FIB, FEI Helios G3 UC) machine using a 30 keV Ga ion beam and transferred to Cu lift-out grids via in situ lift-out technique. In order to prevent charging during FIB preparation, the samples were coated with a 20 nm layer of Au before FIB preparation. The thickness of the lamellae was around 100 nm. An FEI Talos F200X TEM equipped with a high brightness Schottky-FEG (X-FEG) and a four-quadrant SDD-EDS system (solid angle of 0.9 srad) was used for EDS analysis. Spectrum images were obtained using a probe current of 1 nA and a dwell time of 5 µs per pixel. Resolution of the spectrum image is 1024 × 1024 pixels, 1.5 nm in size, resulting in a horizontal field of view of 1.56 µm. Velox (FEI) was used for data acquisition and visualization. For the spectrum images the energies of following elements were used: Al-K_α (1.49 keV), O-K_α (0.52 keV), Ti-K_α (4.51 keV) and N-K_α (0.39 keV).

Supporting Information

Supporting Information is available from the Wiley Online Library or from the author.

Acknowledgements

The authors gratefully acknowledge financial support from the German Research Foundation (DFG) via SFB 986 "Tailor-Made Multi-Scale Materials Systems: M3," Project-ID 192346071, and projects C1, C7, and Z3.

Open access funding enabled and organized by Projekt DEAL.

Conflict of Interest

The authors declare no conflict of interest.

Data Availability Statement

Research data are not shared.

Keywords

high-temperature stability, photonics, plasmonics, thin films, titanium nitride

Received: February 14, 2021
Revised: May 1, 2021
Published online: May 29, 2021

[1] G. Baffou, F. Cichos, R. Quidant, *Nat. Mater.* **2020**, *19*, 946.
[2] A. Naldoni, Z. A. Kudyshev, L. Mascaretti, S. P. Sarmah, S. Rej, J. P. Froning, O. Tomanec, J. E. Yoo, D. Wang, Š. Kment, T. Montini, P. Fornasiero, V. M. Shalaev, P. Schmuki, A. Boltasseva, R. Zbořil, *Nano Lett.* **2020**, *20*, 3663.
[3] S. Ishii, S. L. Shinde, W. Jevasuwan, N. Fukata, T. Nagao, *ACS Photonics* **2016**, *3*, 1552.
[4] M. Chirumamilla, G. V. Krishnamurthy, K. Knopp, T. Krekeler, M. Graf, D. Jalas, M. Ritter, M. Störmer, A. Y. Petrov, M. Eich, *Sci. Rep.* **2019**, *9*, 7241.
[5] N. Jeon, D. J. Mandia, S. K. Gray, J. J. Foley, A. B. F. Martinson, *ACS Appl. Mater. Interfaces* **2019**, *11*, 41347.
[6] R. St-Gelais, G. R. Bhatt, L. Zhu, S. Fan, M. Lipson, *ACS Nano* **2017**, *11*, 3001.
[7] P. Karl, M. Ubl, M. Hentschel, P. Flad, Z.-Y. Chiao, J.-W. Yang, Y.-J. Lu, H. Giessen, *Opt. Mater. Express* **2020**, *10*, 2597.
[8] A. Naldoni, U. Guler, Z. Wang, M. Marelli, F. Malara, X. Meng, L. V. Besteiro, A. O. Govorov, A. V. Kildishev, A. Boltasseva, V. M. Shalaev, *Adv. Opt. Mater.* **2017**, *5*, 1601031.
[9] R. Sakakibara, V. Stelmakh, W. R. Chan, M. Ghebrebrhan, J. D. Joannopoulos, M. Soljacic, I. Čelanović, *J. Photonics Energy* **2019**, *9*, 032713.
[10] D. N. Woolf, E. A. Kadlec, D. Bethke, A. D. Grine, J. J. Nogan, J. G. Cederberg, D. B. Burckel, T. S. Luk, E. A. Shaner, J. M. Hensley, *Optica* **2018**, *5*, 213.
[11] M. Chirumamilla, A. S. Roberts, F. Ding, D. Wang, P. K. Kristensen, S. I. Bozhevolnyi, K. Pedersen, *Opt. Mater. Express* **2016**, *6*, 2704.
[12] N. Jeon, J. J. Hernandez, D. Rosenmann, S. K. Gray, A. B. F. Martinson, J. J. Foley, *Adv. Energy Mater.* **2018**, *8*, 1801035.
[13] A. Fiorino, L. Zhu, D. Thompson, R. Mittapally, P. Reddy, E. Meyhofer, *Nat. Nanotechnol.* **2018**, *13*, 806.
[14] K. Cui, P. Lemaire, H. Zhao, T. Savas, G. Parsons, A. J. Hart, *Adv. Energy Mater.* **2018**, *8*, 1801471.
[15] H. R. Seyf, A. Henry, *Energy Environ. Sci.* **2016**, *9*, 2654.
[16] A. S. Roberts, M. Chirumamilla, D. Wang, L. An, K. Pedersen, N. A. Mortensen, S. I. Bozhevolnyi, *Opt. Mater. Express* **2018**, *8*, 3717.
[17] Y. Li, C. Lin, Z. Wu, Z. Chen, C. Chi, F. Cao, D. Mei, H. Yan, C. Y. Tso, C. Y. H. Chao, B. Huang, *Adv. Mater.* **2020**, *33*, 2005074.
[18] L. Mascaretti, A. Schirato, R. Zbořil, Š. Kment, P. Schmuki, A. Alabastri, A. Naldoni, *Nano Energy* **2021**, *83*, 105828.
[19] S. Rej, L. Mascaretti, E. Y. Santiago, O. Tomanec, Š. Kment, Z. Wang, R. Zbořil, P. Fornasiero, A. O. Govorov, A. Naldoni, *ACS Catal.* **2020**, *10*, 5261.
[20] J. P. Borel, *Surf. Sci.* **1981**, *106*, 1.
[21] D. Peykov, Y. X. Yeng, I. Celanovic, J. D. Joannopoulos, C. A. Schuh, *Opt. Express* **2015**, *23*, 9979.
[22] V. Rinnerbauer, Y. X. Yeng, W. R. Chan, J. J. Senkevich, J. D. Joannopoulos, M. Soljačić, I. Celanovic, *Opt. Express* **2013**, *21*, 11482.
[23] F. Cao, D. Kraemer, L. Tang, Y. Li, A. P. Litvinchuk, J. Bao, G. Chen, Z. Ren, *Energy Environ. Sci.* **2015**, *8*, 3040.
[24] R. Zhang, J. Cohen, S. Fan, P. V. Braun, *Nanoscale* **2017**, *9*, 11187.
[25] J. B. Chou, Y. X. Yeng, Y. E. Lee, A. Lenert, V. Rinnerbauer, I. Celanovic, M. Soljačić, N. X. Fang, E. N. Wang, S.-G. Kim, *Adv. Mater.* **2014**, *26*, 8041.
[26] S. K. Kuk, Y. Ham, K. Gopinath, P. Boonmongkolras, Y. Lee, Y. W. Lee, S. Kondaveeti, C. Ahn, B. Shin, J.-K. Lee, S. Jeon, C. B. Park, *Adv. Energy Mater.* **2019**, *9*, 1900029.
[27] K. Chaudhuri, U. Guler, S. I. Azzam, H. Reddy, S. Saha, E. E. Marinero, A. V. Kildishev, V. M. Shalaev, A. Boltasseva, *ACS Photonics* **2020**, *7*, 472.
[28] W. Li, U. Guler, N. Kinsey, G. V. Naik, A. Boltasseva, J. Guan, V. M. Shalaev, A. V. Kildishev, *Adv. Mater.* **2014**, *26*, 7959.
[29] L. Mascaretti, T. Barman, B. R. Bricchi, F. Münz, A. L.i Bassi, Š. Kment, A. Naldoni, *Appl. Surf. Sci.* **2021**, *554*, 149543.
[30] J. A. Briggs, G. V. Naik, T. A. Petach, B. K. Baum, D. Goldhaber-Gordon, J. A. Dionne, *Appl. Phys. Lett.* **2016**, *108*, 051110.
[31] A. Zeilinger, J. Todt, C. Krywka, M. Müller, W. Ecker, B. Sartory, M. Meindlhumer, M. Stefenelli, R. Daniel, C. Mitterer, J. Keckes, *Sci. Rep.* **2016**, *6*, 22670.
[32] C. Ziebert, S. Ulrich, *J. Vac. Sci. Technol., A* **2006**, *24*, 554.
[33] W.-P. Guo, R. Mishra, C.-W. Cheng, B.-H. Wu, L.-J. Chen, M.-T. Lin, S. Gwo, *ACS Photonics* **2019**, *6*, 1848.
[34] A. Kharitonov, S. Kharintsev, *Opt. Mater. Express* **2020**, *10*, 513.
[35] G. V. Naik, J. L. Schroeder, X. J. Ni, A. V. Kidishev, T. D. Sands, A. Boltasseva, *Opt. Mater. Express* **2012**, *2*, 478.
[36] G. V. Naik, B. Saha, J. Liu, S. M. Saber, E. A. Stach, J. M. K. Irudayaraj, T. D. Sands, V. M. Shalaev, A. Boltasseva, *Proc. Natl. Acad. Sci. USA* **2014**, *111*, 7546.
[37] W. A. Challener, C. Peng, A. V. Itagi, D. Karns, W. Peng, Y. Peng, X. Yang, X. Zhu, N. J. Gokemeijer, Y. T. Hsia, G. Ju, R. E. Rottmayer, M. A. Seigler, E. C. Gage, *Nat. Photonics* **2009**, *3*, 220.
[38] U. Guler, A. Boltasseva, V. M. Shalaev, *Science* **2014**, *344*, 263.
[39] L. Pan, D. B. Bogy, *Nat. Photonics* **2009**, *3*, 189.
[40] S. Ishii, R. P. Sugavaneshwar, T. Nagao, *J. Phys. Chem. C* **2016**, *120*, 2343.
[41] M. Chirumamilla, A. Chirumamilla, Y. Yang, A. S. Roberts, P. K. Kristensen, K. Chaudhuri, A. Boltasseva, D. S. Sutherland, S. I. Bozhevolnyi, K. Pedersen, *Adv. Opt. Mater.* **2017**, *5*, 1700552.
[42] T. Chookajorn, H. A. Murdoch, C. A. Schuh, *Science* **2012**, *337*, 951.
[43] N. Jeon, I. Lightcap, D. J. Mandia, A. B. F. Martinson, *ACS Appl. Mater. Interfaces* **2019**, *11*, 11602.
[44] J. Su, R. Boichot, E. Blanquet, F. Mercier, M. Pons, *CrystEngComm* **2019**, *21*, 3974.
[45] X. Wang, H. Wang, J. Jian, B. X. Rutherford, X. Gao, X. Xu, X. Zhang, H. Wang, *Nano Lett.* **2020**, *20*, 6614.
[46] X. Li, K. Lu, *Nat. Mater.* **2017**, *16*, 700.
[47] P. Mao, J. Qiao, Y. Zhao, S. Jiang, K. Cui, J. Qiu, K. Tai, J. Tan, C. Liu, *Carbon* **2021**, *172*, 712.
[48] R. Ding, Y. Yao, B. Sun, G. Liu, J. He, T. Li, X. Wan, Z. Dai, D. Ponge, D. Raabe, C. Zhang, A. Godfrey, G. Miyamoto, T. Furuhara, Z. Yang, S. van der Zwaag, H. Chen, *Sci. Adv.* **2020**, *6*, eaay1430.
[49] L. Sun, X. He, J. Lu, *npj Comput. Mater.* **2018**, *4*, 6.
[50] K. Lu, *Nat. Rev. Mater.* **2016**, *1*, 16019.
[51] X. Li, Y. Wei, L. Lu, K. Lu, H. Gao, *Nature* **2010**, *464*, 877.
[52] L. Lu, X. Chen, X. Huang, K. Lu, *Science* **2009**, *323*, 607.
[53] D. Sagapuram, Z. Wang, C. Saldana, *Philos. Mag.* **2014**, *94*, 3413.
[54] L. E. Murr, *Phys. Unserer Zeit* **1977**, *8*, 30.
[55] G. W. Nieman, J. R. Weertman, R. W. Siegel, *J. Mater. Res.* **2011**, *6*, 1012.
[56] B. Scherrer, M. Döbeli, P. Felfer, R. Spolenak, J. Cairney, H. Galinski, *Adv. Mater.* **2015**, *27*, 6220.
[57] X. Zhang, A. Misra, *Scr. Mater.* **2012**, *66*, 860.
[58] J. F. Nie, Y. M. Zhu, J. Z. Liu, X. Y. Fang, *Science* **2013**, *340*, 957.
[59] Y. Tian, B. Xu, D. Yu, Y. Ma, Y. Wang, Y. Jiang, W. Hu, C. Tang, Y. Gao, K. Luo, Z. Zhao, L.-M. Wang, B. Wen, J. He, Z. Liu, *Nature* **2013**, *493*, 385.
[60] Q. Huang, D. Yu, B. Xu, W. Hu, Y. Ma, Y. Wang, Z. Zhao, B. Wen, J. He, Z. Liu, Y. Tian, *Nature* **2014**, *510*, 250.
[61] L. Zhang, Y. Wu, W. Yu, S. Shen, *Eng. Anal. Boundary Elem.* **2019**, *105*, 231.
[62] H.-E. Cheng, T.-T. Lin, M.-H. Hon, *Scr. Mater.* **1996**, *35*, 113.
[63] D. P. Field, L. T. Bradford, M. M. Nowell, T. M. Lillo, *Acta Mater.* **2007**, *55*, 4233.
[64] T. LaGrange, B. W. Reed, M. Wall, J. Mason, T. Barbee, M. Kumar, *Appl. Phys. Lett.* **2013**, *102*, 011905.
[65] A. Kahrimanidis, U. Klement, *Mater. Sci. Forum* **2013**, *783-786*, 5.
[66] Z. L. Wang, *J. Phys. Chem. B* **2000**, *104*, 1153.
[67] Y.-N. Wen, J.-M. Zhang, *Solid State Commun.* **2007**, *144*, 163.

[68] R. Chowdhury, N. Biunno, J. Narayan, *MRS Online Proc. Libr.* **1993**, *317*, 199.
[69] D. Gall, S. Kodambaka, M. A. Wall, I. Petrov, J. E. Greene, *J. Appl. Phys.* **2003**, *93*, 9086.
[70] M. Marlo, V. Milman, *Phys. Rev. B* **2000**, *62*, 2899.
[71] A. Chambers, *Modern Vacuum Physics*, CRC Press, Boca Raton, FL **2004**.
[72] F. Wooten, in *Optical Properties of Solids*, Academic Press, San Diego, CA **1972**, p. 1.
[73] H. Reddy, U. Guler, Z. Kudyshev, A. V. Kildishev, V. M. Shalaev, A. Boltasseva, *ACS Photonics* **2017**, *4*, 1413.
[74] H.-Y. Chen, F.-H. Lu, *J. Vac. Sci. Technol., A* **2005**, *23*, 1006.
[75] F. Esaka, K. Furuya, H. Shimada, M. Imamura, N. Matsubayashi, H. Sato, A. Nishijima, A. Kawana, H. Ichimura, T. Kikuchi, *J. Vac. Sci. Technol., A* **1997**, *15*, 2521.
[76] J. Desmaison, P. Lefort, M. Billy, *Oxid. Met.* **1979**, *13*, 505.
[77] J. F. Rekus, *Complete Confined Spaces Handbook*, CRC Press, Boca Raton, FL **1994**.
[78] M. Chirumamilla, G. V. Krishnamurthy, S. S. Rout, M. Ritter, M. Störmer, A. Y. Petrov, M. Eich, *Sci. Rep.* **2020**, *10*, 3605.
[79] G. V. Krishnamurthy, M. Chirumamilla, S. S. Rout, K. P. Furlan, T. Krekeler, M. Ritter, H.-W. Becker, A. Y. Petrov, M. Eich, M. Störmer, *Sci. Rep.* **2021**, *11*, 3330.
[80] J. I. Langford, A. J. C. Wilson, *J. Appl. Crystallogr.* **1978**, *11*, 102.
[81] G. A. Jeffery, *J. Chem. Educ.* **1957**, *34*, A178.
[82] C. García-Meca, R. Ortuño, F. J. Rodríguez-Fortuño, J. Martí, A. Martínez, *Opt. Lett.* **2009**, *34*, 1603.
[83] W. W. Mullins, *J. Appl. Phys.* **1986**, *59*, 1341.
[84] J. F. Shackelford, Y.-H. Han, S. Kim, S.-H. Kwon, in *CRC Materials Science and Engineering Handbook*, 4th ed., CRC Press, Boca Raton, FL **2015**, p. 644.
[85] J. Narayan, B. C. Larson, *J. Appl. Phys.* **2002**, *93*, 278.
[86] S. Gupta, A. Moatti, A. Bhaumik, R. Sachan, J. Narayan, *Acta Mater.* **2019**, *166*, 221.
[87] E. Suhir, in *Handbook of Crystal Growth*, 2nd ed. (Ed: T. F. Kuech), North-Holland Publishing, Boston **2015**, p. 983.
[88] J. W. Christian, S. Mahajan, *Prog. Mater. Sci.* **1995**, *39*, 1.
[89] K. Hattar, in *Nanostructured Metals and Alloys* (Ed: S. H. Whang), Woodhead Publishing, Cambridge, UK **2011**, p. 213.